International Journal of Engineering & Technology, 7 (3.13) (2018) 113-122

International Journal of Engineering & Technology

Website: www.sciencepubco.com/index.php/IJET

Research paper

Two-Phase Fin-Induced Turbulent Cooling for Electronic Devices Using Heat Pump Associated Micro-Gap Heat Sink

Shugata Ahmed[1], Erwin Sulaeman[2*], Ahmad Faris Ismail[2], Muhammad Hasibul Hasan[3]

[1]*Department of Robotics and Mechatronics Engineering, Faculty of Engineering and Technology, University of Dhaka, Dhaka 1000, Bangladesh*

[2]*Departmental of Mechanical Engineering, Faculty of Engineering, International Islamic University Malaysia, Jalan Gombak, 53100, Kuala Lumpur, Malaysia*

[3]*Departmental of Mechanical and Industrial Engineering, Faculty of Engineering and Architectural Science, Ryerson University, 350 Victoria Street, Toronto, ON 5MB 2K3, Canada*

**Corresponding author E-mail: esulaeman@iium.edu.my*

Abstract

High energy requirement for electronic cooling is a major problem to operate high performance computers and data centres. Developing low cost thermal management systems for micro-electronic devices and micro-electro-mechanical systems (MEMS) is a cutting edge research area. A heat pump system associating micro-gap evaporator with internal micro-fins is a potential candidate for two-phase cooling of these advanced devices. Micro-fins induce pseudo-turbulence in the flow field, which escalates heat transfer rate. In this paper, the system performance of a heat pump using micro-gap evaporator has been investigated numerically and experimentally. As heat transfer rate in the micro-gap evaporator is influenced by turbulence generation, flow field in the inlet and outlet manifolds have been visualized in the numerical simulation to observe fin-induced pseudo-turbulence at the entrance and outlet of the micro-gap evaporator. The simulation has been performed using FLUENT 14.5 release. Experimental work has been carried out to validate numerical results. For experimentation purpose, a test rig has been developed, which contains a test section accommodating the micro-gap evaporator. A heater is provided at the bottom of the evaporator to supply uniform heat flux ranging 1 ~ 8 kW/m^2. A pre-heater is installed at the compressor outlet to vary refrigerant temperature at the condenser inlet. The range of pre-heater temperature is 93 ~ 159°C. A variable speed compressor is used. The input frequency to the compressor is varied within the range of 20 ~ 50 Hz to run the compressor at different speeds. Experimental data show good agreement with numerical results. It is observed that in transient state, temperatures and pressures at different locations of the test apparatus fluctuate due to quasi-periodic dry out and surface rewetting nature of the flow. When pre-heater temperature is set at 159^0 C and compressor frequency is increased from 20 Hz to 30 Hz, evaporator wall heat flux escalates 118.2% and heat transfer rate of the condenser increases 65.2%. However, heat transfer rate declines with the further increment of compressor frequency. Coefficient of performance (COP) of the heat pump also increases with the frequency increment from 20 Hz to 30 Hz and declines after surpassing 40 Hz frequency.

Keywords: *Micro-gap evaporator; micro-fin; pseudo-turbulence; flow boiling; heat pump; coefficient of performance*

1. Introduction

Micro-scale cooling is one of the potential thermo-fluidic applications and a cutting-edge research area due to its applicability in diverse fields of engineering and technology. Micro-gap evaporators are promising candidates of micro-scale cooling. The scope of applications of micro-gap evaporator is in thermal management of micro-electronic devices, micro-electro-mechanical systems (MEMS)/ micro-opto-electro-mechanical systems (MOEMS), micro-opto-electronic devices such as photovoltaic cells, image sensors, laser diodes etc., micro-electro-chemical devices such as fuel cells and batteries and micro-reactors [1,2].

Previously, heat transfer performance of microchannels have been investigated by many researchers. Microchannels offer high performance heat sinking for micro-scale devices. High heat dissipation capability of microchannels is originated from its large heat transfer surface-to-volume ratio. This advantageous characteristics of microchannel was noted first by Tuckerman and Peace [3] for electronic cooling. They found that dissipated heat flux from a 60 µm wide and 302 µm deep channel is up to 790 W/cm^2, while using water as working fluid. However, pressure drop in microchannel is high, which elevates pumping power requirement. Later researches were carried out on evaporative cooling performance of micro-channels. Many researchers reported that heat flux removal rate during flow boiling is much higher than single-phase cooling [4, 5]. However, two-phase flow in microchannels exhibits some disadvantages such as flow boiling instabilities, flow reversal, exceeding critical heat flux (CHF) and hot spot generation [6, 7]. Although flow boiling has several drawbacks, it is essential for high performance cooling such as cooling of nuclear reactors. Hence, reducing prevailing two-phase problems is a cutting edge research area.

Micro-gap heat sinks have been studied by researchers to minimize flow boiling associated problems. Alam et al. [8] showed that for high heat flux and low mass flow rate, micro-gaps have higher heat transfer capability compared to microchannel heat

Copyright © 2018 Authors. This is an open access article distributed under the Creative Commons Attribution License, which permits unrestricted use, distribution, and reproduction in any medium, provided the original work is properly cited.

sinks. They depicted that confined slug and annular flow regimes are dominant flow patterns in micro-gaps. Kim et al. [9], Barcohen and Rahim [10] also perceived annular flow patterns in micro-gap heat sinks. Alam et al. [11] investigated heat transfer and pressure drop characteristics of three different micro gaps of 190 µm, 285 µm and 381 µm heights. Experimental results showed that heat transfer coefficient increases with the decrement of gap size. On the other hand, pressure drop is higher for smaller gap sizes. However, in another publication, Alam et al. [12] stated that below 100 µm, dry out takes place very early. Hence, it is not suitable for cooling purpose. They showed that the gap size should be between 100-500 µm for effective cooling.

Internal micro-fins are used to enhance heat transfer rate in micro-gaps. For this reason, micro-fins are used in heat exchangers, heat pipes, heat sinks and many other high temperature applications [13]. Yeom et al.[14] remarked that micro-fins improve boiling and condensing surfaces. Fins not only extend surface area but also generate turbulence [15]. Hence, convective heat transfer rate augments by rapid fluid mixing.

Previous works of these authors introduced the concept of integrating micro-fins with micro-gap heat sinks for two-phase heat transfer enhancement [16-19]. However, only numerical results were presented in these papers. It was found that micro-finned micro-gaps are suitable for high heat flux applications [16]. Rectangular fin micro-gap has superior heat transfer capability to that of triangular fin profile [17]. However, pressure drop and wall shear stress development was also higher than that of triangular finned gap. It was shown that heat transfer rate and pressure drop are influenced by geometrical parameters [18]. In another publication, turbulence characteristics of flow boiling micro-finned micro-gap are briefly discussed [19].

In literature, experimental investigation on performance of heat pump using micro-finned micro-gap evaporator has not been presented yet. Moreover, visualization of pseudo-turbulence in simulation has not been found in previous works.

The objective of this paper is to investigate system performance of a heat pump with a micro-gap evaporator accommodating internal micro-fins of rectangular profile, compressor, condenser and capillary tube. Coefficient of performance (COP) of the system has been calculated, which depends on heat transfer in the evaporator and power consumed by the compressor. Hence, it is necessary to study heat transfer performance of the evaporator. The wall heat flux in the evaporator section has been investigated as a function of average wall temperature, pre-heater temperature and compressor frequency. Transient behavior of the system has also been explored, which includes temperature and pressure fluctuations at different sections of the setup. Temperature and pressure fluctuation occur due to unstable fluid flow. To explain the transient results, flow has been visualized at the inlet and outlet manifolds of the test section.

Heat transfer in the evaporator is greatly improved by turbulence generation. The role of micro-fins in turbulence generation are investigated by numerical simulation. As turbulence is generated at the entrance and outlet of the micro-gap evaporator, flow field in the inlet and outlet manifolds as well as in the channel have been visualized and turbulence intensity ratio has been plotted.

2. Two-Phase Flow and Turbulence Modeling

2.1 Governing Equations

Volume of Fluid (VOF) model, proposed by Hirt and Nichols [20], has been used for multiphase flow modeling. In VOF model, a single-set of momentum equations has been solved for both phases and volume fraction of each phases are tracked throughout the domain. Governing equations used in VOF model are given. The continuity equation:

$$\frac{\partial(\alpha\rho_v)}{\partial t} + \nabla.(\alpha\rho_v\vec{v}_v) = m_{evp} \quad (1)$$

Here ρ_v and $\vec{v}_v$ are density and velocity of vapor respectively, α is the void fraction and m_{evp} represents mass transfer rate from liquid to vapor phase. In VOF model, void fraction α is defined by the following equation:

$$\alpha = \frac{1}{V}\int_V I(x,t)dV \quad (2)$$

Here $I(x,t)$ is known as the marker function, which is a multidimensional unit step function. In primary phase, value of the marker function is 1, while in secondary phase it is 0. By solving Eq. (2), distribution of void fraction α is obtained in the flow domain. Later volume fraction distribution of liquid phase is calculated from (*1- α*). For steady-state condition, $\frac{\partial\alpha}{\partial t} = 0$.

Conservation of momentum equation:

$$\frac{\partial(\rho\vec{v})}{\partial t} + \nabla.(\rho\vec{v}\vec{v}) = -\nabla P + \nabla\tau + \rho\vec{g} + \vec{F} \quad (3)$$

Here ∇P and $\nabla\tau$ are pressure and shear stress gradients, respectively. $\vec{g}$ is the gravitational acceleration and $\vec{F}$ denotes the surface tension force. For Newtonian fluid, shear stress is expressed as following:

$$\tau = \mu[\nabla\vec{v} + (\nabla\vec{v})^T] \quad (4)$$

In this equation, μ is the dynamic viscosity of the mixture. Mixture properties are defined by following formulas:

Density: $\rho = \alpha\rho_l + (1-\alpha)\rho_v$ (5)

Dynamic viscosity: $\mu = \alpha\mu_l + (1-\alpha)\mu_v$ (6)

Continuum surface force (CSF) method [21] has been used to calculate the surface tension force. The equation is the following:

$$F = \sigma\kappa\nabla\alpha \quad (7)$$

Here, σ is surface tension coefficient and κ is local curvature of liquid-vapor interface. Surface normal at the interface is defined as gradient of void fraction:

$$n = \nabla\alpha \quad (8)$$

Then surface curvature κ is the following:

$$\kappa = \nabla.\hat{n} \quad (9)$$

where unit normal, $\hat{n} = \frac{n}{|n|}$.

Conservation of energy equation for fluid domain is written as:

$$\frac{\partial(\rho E)}{\partial t} + \nabla.\left(\vec{v}(\rho E + P)\right) = \nabla.\left(k_{eff}\nabla T\right) \quad (10)$$

Here E and T are mass-averaged energy and fluid temperature, respectively. k_{eff} represents effective thermal conductivity.

For solid domain, the energy equation can be written as:

$$\nabla(k_s\nabla T_s) = \frac{\partial(\rho_s c_{p,s} T_s)}{\partial t} \quad (11)$$

Here, k_s, ρ_s, $C_{p,s}$ and T_s are thermal conductivity, density, specific heat capacity and temperature of solid material, respectively.

As stated earlier, fins are responsible for generating turbulence. Hence, a turbulence model is necessary for complete flow modeling. Renormalization Group Theory (RNG) *k-ε* turbulence model

[22] has been used to simulate the turbulent flow. Governing equations for turbulence are given below.
Equation to calculate turbulence kinetic energy:

$$\frac{\partial k}{\partial t} + \nabla(\vec{v}.k) = \frac{1}{\rho}\left[\nabla\left(a_k.\mu_{eff}.\nabla k\right) + G_k + G_b - \rho\varepsilon - Y_M + S_k\right] \quad (12)$$

Equation for turbulence kinetic energy dissipation rate:

$$\frac{\partial \varepsilon}{\partial t} + \nabla(\vec{v}.\varepsilon) = \frac{1}{\rho}\left[\nabla\left(a_\varepsilon.\mu_{eff}.\nabla\varepsilon\right) + C_{1\varepsilon}\frac{\varepsilon}{k}(G_k + C_{3\varepsilon}G_b) - C_{2\varepsilon}\rho\frac{\varepsilon^2}{k} - R_\varepsilon + S_\varepsilon\right] \quad (13)$$

In above equations, k and ε are turbulence kinetic energy and rate of energy dissipation, respectively. G_k and G_b are generation of turbulence kinetic energy due to the mean velocity gradients and buoyancy, respectively. Y_M term includes contribution of the fluctuating dilatation in compressible turbulence to the overall dissipation rate. a_k and a_ε are inverse effective Prandtl numbers for k and ε, respectively and S_k and S_ε are source terms. The model constants have following default values [22]:

$C_{1\varepsilon}$ = 1.42, $C_{2\varepsilon}$ = 1.68

Orszag et al. [22] determined these coefficient values from numerous iterations of data fitting for a wide range of turbulent flows.

2.2 Interfacial Temperature Condition

Interface temperature condition is critical. According to Schrage [23], at thermodynamic equilibrium condition, a temperature jump at the interface exist due to pressure difference between vapor and bulk fluid. Hence, temperature condition at the interface can be written as: $T_{sat(P_l)} = T_l \neq T_v = T_{sat(P_v)}$. To employ this condition in mathematical model is a challenge. In numerical simulation, the saturation temperature should be maintained at the interface, which is correlated with the mass transfer between two phases occurs at the interface. It is discussed in the next section.

2.3 Modeling Mass Transfer

Mass exchange between two phases is calculated from evaporation-condensation model, proposed by Lee [24]. Following equation is used:

$$m_{evp} = coeff * (1-\alpha)\rho_l\frac{(T_l - T_{sat})}{T_{sat}} \quad (14)$$

In this equation, the value of evaporation coefficient should be defined to maintain saturation temperature (T_{sat}) at the interface. Wu et al. (2007) [25], De Schepper et al. (2009) [26] and Alizadehdakhel et al. (2010) [27] recommended that the value of evaporation coefficient should be 0.1 to satisfy the criterion.

2.4 Boundary Conditions

Various boundary conditions are defined at inlet, outlet and outer walls of the heat sinks, which are stated below:
Inlet: $T_f = T_{in}$, $v = v_{in}$, $\alpha = \alpha_{in}$.
Turbulence intensity is also defined at the inlet. For fully developed internal flow, turbulence intensity is calculated from following formula:

$$I = \frac{u'}{u_{avg}} = 0.16(Re)^{-\frac{1}{8}} \quad (15)$$

Here, u' = root mean square of velocity fluctuations, u_{avg} = mean flow velocity and Re = Reynolds number.
Outlet: $P = P_{out}$. Atmospheric pressure is defined at the outlet of the heat sink.
Solid-fluid interface: Heat transfer from wall to fluid is by convection. Convective heat transfer coefficient is calculated from the following equation:

$$h = \frac{Q_{eff}}{A_f(T_s - T)} \quad (16)$$

Here, h is convective heat transfer coefficient, Q_{eff} is heat transfer rate by convection, A_f is the surface area, T_s and T are temperature of solid and fluid, respectively.
Channel bottom wall: Uniform heat flux is applied at the bottom of the heat sink. Heat is transferred through solid wall by conduction in the normal direction of the bottom surface. Heat flux transferred by conduction is calculated from the following equation:

$$q = -k_s\frac{\partial T_s}{\partial n} \quad (17)$$

Other channel walls: Other channel walls are considered as insulated. Hence, $q_{loss} = 0$. As a result, temperature gradient at boundaries:

$$\frac{\partial T_s}{\partial n} = 0 \quad (18)$$

3. Numerical Solution

Hybrid meshes with different element numbers have been created by ANSYS Workbench. Minimum number of elements should be considered in the simulation to minimize computational time. To find out optimum number of elements, grid independent test (GIT) has been carried out by observing area-weighted average surface Nusselt number (Nu_{avg}) and calculating corresponding relative error for different numbers of meshing elements. Relative error = (Nu_{max} – Nu_{avg})/Nu_{max}, where Nu_{max} is the maximum Nusselt number calculated from simulation results. Table 1. shows GIT results. As the grid with 1,986,236 number of elements possesses small relative error, it has been used in the simulation.

Simulation has been carried out using FLUENT 14.5 release solver. The governing equations are solved by finite volume method. The conservation of momentum equation involves both pressure and velocity field. If neither fields are specified, an iterative procedure should be followed to determine pressure and velocity fields. In this study, Semi-Implicit Method for Pressure Linked Equations (SIMPLE) algorithm [28] has been used to solve pressure velocity coupling equation. In this procedure, a velocity field is estimated from a guessed pressure field (p^*). The validity of the estimated velocity is checked from the criterion that it must satisfy the continuity equation. If not satisfied, a pressure correction equation is solved and estimated velocity is corrected from pressure correction field. The procedure is repetitive until convergence is achieved.

Table 1: GIT results

No. of elements	Nu_{avg}	Relative error %
503202	19.9195	19.19
752756	20.188	18.10
1222898	22.268	9.29
158722	23.433	4.94
1986236	24.632	7.71×10^{-4}
2337298	24.651	--------

4. Experimental Setup

The test setup consists of a heat pump and a test section. The working fluid is R-134a. The major components of the heat pump are hermetically sealed low back pressure compressor, condenser with a cooling fan, evaporator and capillary tube. Schematic diagram of the test loop is shown in Fig.1. When refrigerant flows through the evaporator, it receives heat and evaporates at a low temperature. Further, refrigerant vapor is compressed by the compressor to increase pressure as well as its saturation temperature. After that high temperature gas flows to the condenser, where it rejects heat and changes phase from vapor to liquid. Finally, liquid refrigerant flows through the capillary tube to decrease pressure before entering to the evaporator.

The test section is an acrylic structure with inlet and outlet manifolds, which accommodates the heater and the evaporator. All other components of the heat pump are installed at the outer circuit of the test section. The condenser is covered by a polystyrene duct. A cooling fan is provided for forced convective cooling of refrigerant gas in the condenser. 6 K-type thermocouples measure inlet and outlet temperatures of the duct. Air velocity in the duct is measured by an anemometer.

Three pressure gauges are installed at different locations in the circuit to measure gauge pressures. Pressures are measured at compressor, condenser and evaporator outlets. A flow meter from Omega Engineering (FLR 1000-D) measures flow rate of the refrigerant vapor at evaporator outlet. The evaporator and the connecting copper tubes are well covered by polyurethane foam to minimize heat loss.

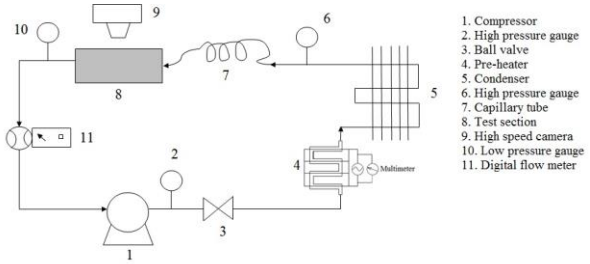


Fig. 1: Schematic diagram of the test rig (main components)

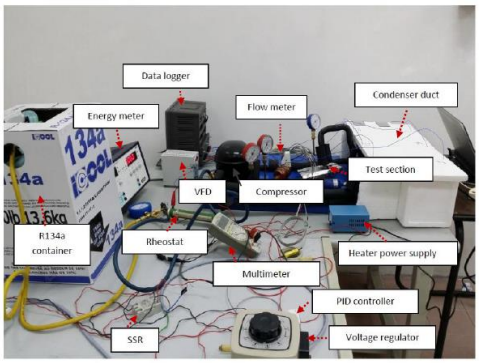


Fig. 2: Experimental setup (main components and accessories)

The micro-gap heat sink does not allow optical access. Hence, flow inside it cannot be visualized. Instead of that, flow visualization has been performed at inlet manifold using a high definition and high speed digital microscopic camera (zoom: 50x-500x). The camera captures flow images of 640×480 pixels at 1200 fps speed. Proper controlling systems are provided to control various input parameters. A coil heater with proportional-integrated-derivative (PID) controller controls refrigerant temperature at the outlet of the compressor. The purpose of the pre-heater is to vary temperature of the refrigerant at the condenser inlet. Heat transfer rate at the condenser is affected by refrigerant temperature at the condenser inlet, which in turn affects coefficient of performance (COP).

Temperatures are recorded using a data logger. Flow rate can be regulated either by controlling compressor frequency using a variable frequency drive (VFD) or operating a ball valve installed at the outlet of the compressor. Volumetric flow rate of refrigerant vapor at the outlet of the test section is acquired using a separate data acquisition system and plotted directly by TracerDAQ software installed in the connected computer. Fig.2 shows a photograph of the experimental setup. Detail specifications of the experimental setup are listed in Table 2 and range of operating conditions are given in Table 3.

Table 2: Specifications of test apparatus

Components	Specifications
Test section	Material: acrylic, inlet and outlet pressure port dia: 6.5 ±0.3 mm
Copper tubes	OD: 6.5±0.1 mm, ID: 5.5±0.1 mm
Peltier heater	Dimension: 30 mm × 30 mm, Power: 400 W
Compressor	Type: hermatically sealed low back pressure, Power: 110 W, Frequency: 50 Hz
Pre-heater	ID: 6.5 mm, Length: 50 mm, Power: 200 W, Resistance: 274 Ω
Microscopic camera	Pixels: 640×480, speed: 1200 fps, zoom: 50x-500x
Thermocouples	K-type, tip dia: 0.1 mm
Flow meter	Brand: Omega Engineering (FLR 1000-D), Accuracy: ±3% FS, Pressure Rating: 40 psi at 20°C for gas

Table 3: Range of operating conditions

Controllable parameters	Units	Range
Heat flux	kW/m^2	1-8
Compressor frequency	Hz	20-50
Pre-heater temperature	˚C	93-159

4.1 Test Section

The test section provides housing for the micro-gap evaporator. The micro-gap with 48 internal micro-fins of rectangular shape has been fabricated by wire-cut electric discharge machining (EDM) on aluminum substrate. Fabricated evaporator has a footprint area of 30 mm × 30 mm. Lower and upper base thicknesses 1 mm and the gap height is 2 mm. Each micro-fin has height and width of 0.3 mm. Fabricated micro-finned micro-gap has been shown in Fig.3(a) and its Scanning Electron Microscopic (SEM) image with dimensions is given in Fig.3(b). The dimensional details are given in Table 4. The heat sink is installed inside of the test section. Acrylic is used as test section material as it can sustain high temperature. At atmospheric pressure, the deflection temperature of acrylic is ~97°C. Moreover, it permits optical access to visualize the flow. The test section has two parts. Lower part of the test section consists of an inlet and outlet manifold and a Peltier heater. The Peltier heater is a solid state device, which transfers heat from one side to other by consuming electrical energy. The heat sink is placed on top of the hot surface of Peltier heater ensuring that it receives heat.

Power supply to the heater is provided from a DC power source. Although a constant 12V DC voltage is applied, the heater power is varied by changing current in the circuit using a rheostat. Wall temperature is varied by varying heater power, which in turn affects the wall heat flux. Heater power is measured by using a multimeter.

Inlet and outlet copper tubes have been inserted in the test section by drilling in the upper part. The upper and lower parts are joined together by screws. Proper sealing has been provided between two parts to avoid any leakage. Total 6 K-type thermocouples of 1 mm tip diameter are attached to upper and lower bases of the heat sink to measure wall temperatures. Two other thermocouples measure inlet and outlet temperatures of the refrigerant. Different parts of the test section are illustrated in Fig.4.

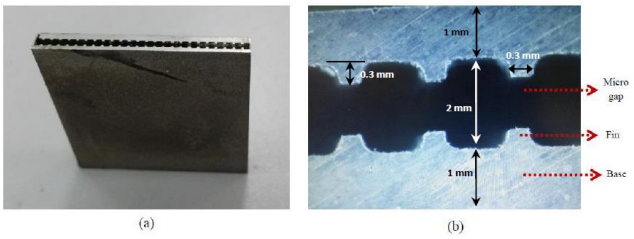


Fig. 3: (a) Fabricated micro-finned micro-gap and (b) SEM image of micro-finned micro-gap with dimensions

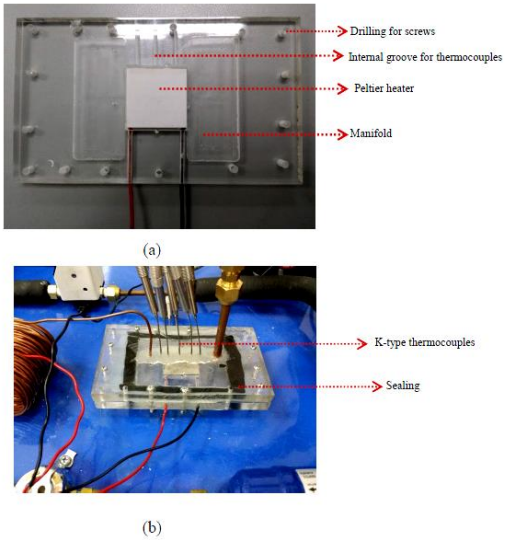


Fig. 4: (a) Lower part of the test section with inlet and outlet manifolds and Peltier heater; (b) complete test section

Table 4: Dimensional details of micro-gap evaporator

Dimension	Unit	Measurement
Footprint area	mm^2	900
Gap height	mm	2
Upper base thickness	mm	1
Lower base thickness	mm	1
Hydraulic diameter	mm	1.11
Number of fins	-	48
Fin height	mm	0.3
Fin width	mm	0.3

4.2 Data Reduction

After performing the tests, heat transfer and fluid flow parameters are calculated from experimental data using relevant formulas. Power supply to the heater is calculated from following equation:

$$Q = I \times V \tag{19}$$

Here, Q is the heater power, I is the current and V is the voltage applied across the heater terminals. Hence, heat flux applied at the bottom of the heat sink:

$$q_{in} = \frac{Q}{A} \tag{20}$$

Here, A = footprint area of the heat sink = $30\text{mm} \times 30\text{mm}$. Wall heat flux:

$$q^{"} = q - q_{loss} \tag{21}$$

Heat loss from the boundaries of the test section (q_{loss}) is obtained from heat loss characterization curve.

The coefficient of performance is the ratio of heat transfer rate at the evaporator-to-compressor power. It is defined by the following formula:

$$COP = \frac{Q_{eff}}{PW} \tag{22}$$

Here, Q_{eff} is the heat transfer rate at the evaporator and PW is the compressor power.

Rate of heat loss in the condenser is calculated from the following equation:

$$Q_{condenser} = \rho_{air} A_{cs_duct} v_{air} \left(T_{out_avg} - T_{in_avg}\right) \tag{23}$$

Here, ρ_{air} is air density at room temperature, A_{cs_duct} is the cross-sectional area of the condenser duct, v_{air} is air velocity measured by anemometer. T_{in_avg} and T_{out_avg} are inlet and outlet temperature averages, respectively. Dimensionless numbers are calculated from following formulas:

Biot number, $Bi = \frac{hD_h}{k_s}$ (24)

Reynolds number, $Re = \frac{\rho_f v L}{\mu}$ (25)

L is the characteristics length of the channel, k_s is the thermal conductivity of channel material. In this study, vapor Reynolds number is calculated from vapor velocity (v_v) at evaporator outlet. Vapor velocity is obtained from volumetric flow rate of vapor:

$$v_v = \frac{\dot{V}_v}{A_{cs}} \tag{26}$$

Here, $\dot{V}_v$ is the volumetric flow rate of vapor measured by the flow meter installed at evaporator outlet and A_{cs} is the cross-sectional area of the evaporator. Hence, vapor Reynolds number:

$$Re_v = \frac{\rho_v \dot{V}_v L}{A_{cs} \mu_v} \tag{27}$$

4.3 Uncertainty Analysis

The experimental error has been analyzed by using Kline and McClintock method [29]. It considers that when a certain variable, R from a certain test is obtained, it should be considered as a function of other variables that measured in the test, known as independent variables. The error value of Biot number (Bi) and vapor Reynolds number (Re_v) are calculated. For Biot number, the independent variables are h and k_s. So the uncertainty equation can be written as:

$$U_{Bi} = \left[\left(\frac{\partial Bi}{\partial h} U_h\right)^2 + \left(\frac{\partial Bi}{\partial k_s} U_{k_s}\right)^2\right]^{1/2} \tag{28}$$

The uncertainties of ρ_v, v_v and μ_v quantities are included in vapor Reynolds number (Re_v). Hence, the uncertainty equation for Re_v is the following:

$$U_{Re_v} = \left[\left(\frac{\partial Re_v}{\partial \rho_v} U_{\rho_v}\right)^2 + \left(\frac{\partial Re_v}{\partial v_v} U_{v_v}\right)^2 + \left(\frac{\partial Re_v}{\partial \mu_v} U_{\mu_v}\right)^2\right]^{1/2} \tag{29}$$

The maximum error obtained for Biot number (Bi) and vapor Reynolds number (Re_v) were 3.02% and 4.53 %, respectively.

5. Heat Loss Characterization

When the system is heated, some amount of heat is lost to the environment through system boundaries although proper insulation is provided. To calculate effective heat flux, heat loss (q_{loss}) from the system need to be determined. In the experiment, refrig-

erant was completely drained out from the test loop using a suction pump. Then the heat sink was heated with different heating powers and corresponding wall temperatures were recorded after achieving steady-state condition. As there is no fluid in the system, all applied heat flux is lost. Fig.5 represents heat flux loss vs. average wall temperature graph. Following linear relationship was obtained:

$$q_{loss} = 82.56 \times T_{wall,avg} - 1848.6 \quad (30)$$

From this equation, heat loss can be calculated for measured wall temperatures during fluid flow.

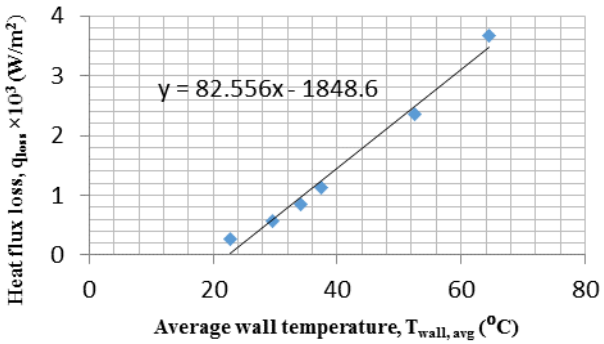


Fig. 5: Heat loss characterization curve

6. Validation of Numerical Results

Adequacy of numerical results has been verified by comparing them with experimental data. In numerical analysis, vapor Reynolds number (Re_v) has been calculated from evaporation rate (m_{evp}). Fig.6(a) shows the Biot number vs. vapor Reynolds number plot for both numerical and experimental results, which provides a good agreement between them. Heat flux ratio $\left(\bar{q} = \frac{q''}{q_{in}}\right)$ is considered 1. The plot shows that Biot number decreases sharply for increasing vapour Reynolds number from 900 to 1400. However, decrement rate slows down after exceeding Re_v=1400. As Re_v depends on evaporation rate, micro-gap is occupied by larger amount of vapor for higher Re_v. Vapor has lower convective heat transfer coefficient, which gives rise to convective thermal resistance. Hence, Biot number, which is the ratio of conductive and convective thermal resistance, subsides.

Another plot of pressure drop (ΔP) vs. vapor Reynolds number, given in Fig.6(b), provides a good validation of numerical results. Similar to Biot number, pressure drop also diminishes with escalating Re_v. Refrigerant vapor possesses lower density than liquid phase. For this reason, frictional pressure drop is lower for higher Reynolds number.

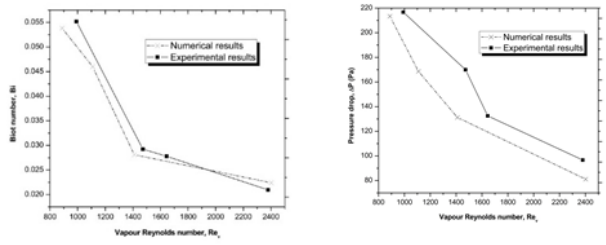


Fig. 6: (a) Plot of Biot number against vapour Reynolds number and (b) Pressure drop vs. vapour Reynolds number plot for numerical and experimental results when $\bar{q} = 1$

7. Results and Discussion

Turbulence generation in micro-gap is a challenging but highly beneficial task as it improves heat transfer coefficient significantly. In microchannels, obstacle arises from confined domain, which restricts the flow to be scattered. As micro-gaps are wider than microchannels, it is more suitable to produce turbulence. Internal micro-fins promote pseudo-turbulence in micro-gaps by inducing supplementary agitation. Inlet and outlet manifolds are also responsible for provoking pseudo turbulence at entrance and exit regions of the heat sink. In Fig.7(a), a divergence in the velocity vector field is notable at micro-gap inlet. On the other hand, a vortex is found at the lower part of the outlet manifold, shown in Fig.7(b).

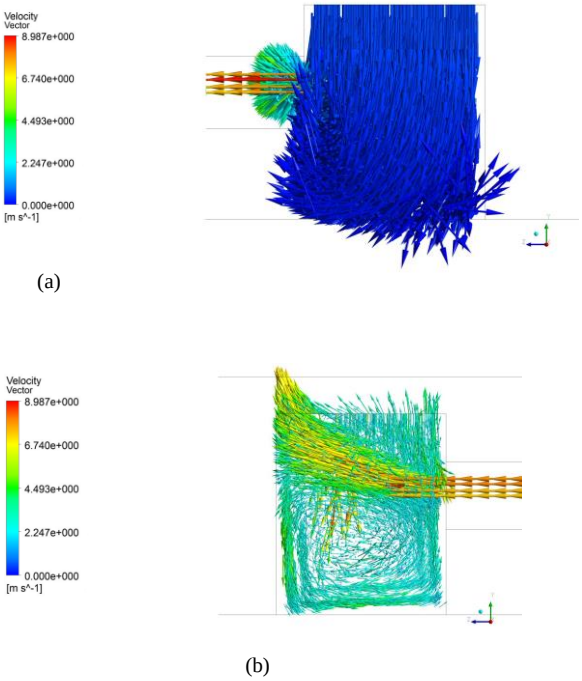


Fig. 7: Velocity vector at (a) Inlet manifold and channel entrance (b) channel exit and outlet manifold for Re=1400, q_{in}=3×10^6 W/m^2 and α_{in}=0

During turbulent flow, local velocity is fluctuated from mean velocity. Ratio of root mean square velocity fluctuation (u') and mean velocity (u) is defined as turbulence intensity ratio (I). In numerical simulation, turbulence intensity ratio is defined at the inlet using Eq.15. Vlahostergios et. al. [30] reported that increment of turbulence intensity results heat transfer enhancement. Hence, it is necessary to examine turbulence intensity distribution in micro-gap. Fig.8 illustrates the turbulence intensity ratio distribution along the length of the heat sink at a constant Reynolds number (Re=1400), heat flux (q_{in}=3×10^6 W/m^2) and inlet vapor quality (α_{in}=0). As turbulence is generated at inlet and outlet zones of the heat sink, gradient of turbulence intensity ratio is found higher in these areas. From figure, it is perceptible that turbulence intensity ratio increases steeply from channel inlet to half of the channel length and then maintains almost constant value. Again, a sudden rise of I value from 1.38 to 1.57 is recognized at the channel exit.

Fig.7. Velocity vector at (a) Inlet manifold and channel entrance (b) channel exit and outlet manifold for Re=1400, q_{in}=3×10^6 W/m^2 and α_{in}=0.

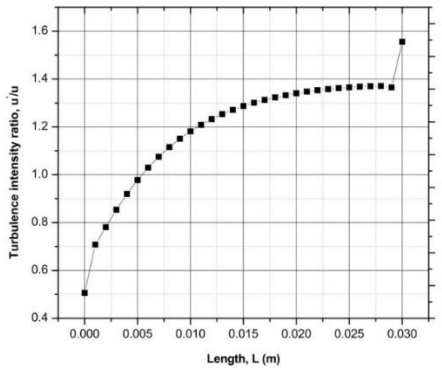


Fig. 8: Turbulence intensity ratio distribution for Re=1400, q_{in}=3×10^6 W/m^2 and α_{in}=0.4

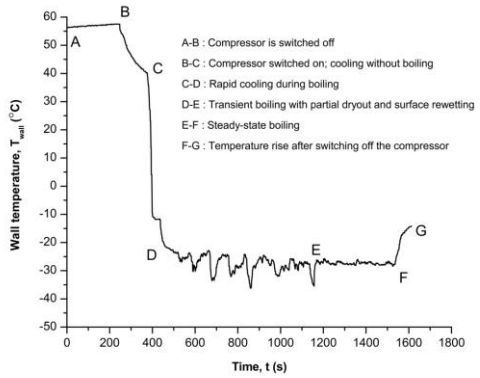


Fig. 9: Wall temperature variation with time for 40 Hz compressor frequency and 3677 W/m^2 heat flux applied

7.2 Experimental Results

In experimental results section, both transient and steady-state results are included. The transient results are presented as flow boiling instabilities. It shows that the wall temperature, condenser inlet and outlet temperature and vapor flow rate at evaporator outlet fluctuate with time. Type of boiling in evaporator is predicted from the boiling curve. In steady-state condition, heat transfer rate and coefficient of performance (COP) are estimated for different compressor frequencies and pre-heating temperatures.

7.2.1 Flow boiling instabilities

Instabilities in different measured parameters are common during flow boiling analysis. Many other researchers such as Wang et al. [31] ,Wu and Cheng [32] and Hetsroni et al. [33] reported instabilities in temperatures and pressures during two-phase flow. Yin et al. [34] documented void fraction fluctuation during flow boiling.

In Fig.9, evaporator wall temperature has been plotted against time, while heat flux, compressor frequency and pre-heater temperature are kept constant. It is perceived that after switching on the compressor, temperature decreased from 60°C to 40°C in 200 seconds. After that, boiling was initiated and temperature sharply dropped to -22°C within a very short period of time. However, at this stage, boiling was unsteady. Quasi-periodic partial dry out and surface rewetting were observed in the inlet manifold, which have been shown in Fig.10. Due to this, evaporator wall temperature response was fluctuating. Wall temperature elevated during partial dry out and again dropped off after rewetting the surface. Finally, wall temperature became steady after 900 second. At 1300 second, compressor was switched off and temperature started to rise.

Condenser inlet and outlet temperature, vapor flow rate and pressure at outlet positions of compressor (P_1) and condenser (P_2) were monitored with time at a constant heat flux, compressor frequency and pre-heater temperature. From Fig.11(a), it is observed that inlet temperature remained almost constant at 25°C. However, outlet temperature started to fluctuate after incipience of boiling.

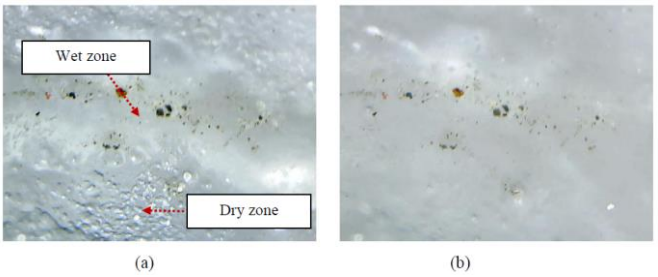


Fig. 10: Flow at inlet manifold - (a) quasi-periodic partial dry out and (b) surface rewetting

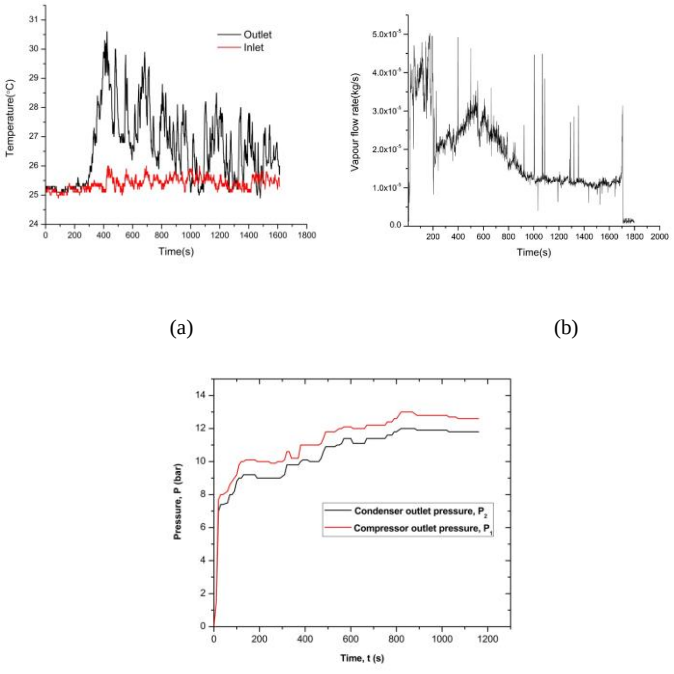


Fig. 11: Flow boiling instabilities: Fluctuation of (a) condenser inlet and outlet temperatures; (b) vapor flow rate at evaporator outlet; (c) pressures at condenser and compressor outlets; (ω=40 Hz, q_{in}=3677 W/m^2)

In Fig.11(b), vapor flow rate vs. time graph has been plotted. In transient state, vapor flow rate at the outlet of the test section also fluctuates with time. As vapor flow rate is related to evaporation rate, it can be predicted that vaporization in the evaporator is inconsistent at this stage. Fig. 11(b) shows that flow rate is high before initiation of boiling at 200 second.

Initially, just after turning on the compressor, system pressure is low. Compressor takes some time to develop pressure in the fluid circuit. Due to low pressure refrigerant exists only in vapor phase. As there is no liquid phase, no boiling occurs at this stage. Refrigerant flows only as vapor through the evaporator and flow rate is recorded by the flow meter installed at the outlet of the evaporator. However, due to unsteady vapor flow, fluctuation is high. After incipience of boiling, the flow rate decreases although instability continued until steady boiling is achieved at 900 second. At steady-state condition, vapor flow rate is minimum.

In Fig.11(c), pressure at outlet positions of compressor (P_1) and condenser (P_2) were plotted against time. It is seen that after switching on the compressor, the pressures in both locations rise sharply over 7 bar. After that in 200s, P_1 and P_2 increase to 10 bar and 8 bar, respectively. During transient boiling period from 200s to 900s, pressures were observed to be fluctuating, which stabilizes after achieving steady-state condition.

7.2.2 Boiling Curve

Predicting a boiling curve provides an insight of two-phase heat transfer corresponding to boiling status. To obtain the boiling curve, average wall temperature ($T_{wall,\ avg}$) is varied by varying heat flux (q_{in}), while compressor frequency (ω) and pre-heater temperature (T_{heater}) are kept constant. Boiling curve obtained from current study is provided in Fig.12. It attributes that wall heat flux (q'') ascends with escalating average wall temperature ($T_{wall,avg}$). From this observation, it can be predicted that corresponding mechanism of heat transfer is nucleate boiling. However, critical heat flux (CHF) could not be achieved due to limited heater capacity.

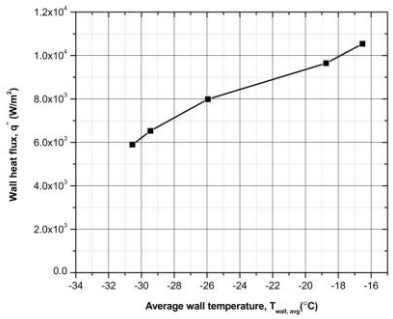


Fig. 12: Boiling curve for 40 Hz frequency

7.2.3 Heat transfer

In Fig.13, heat transfer rate in the condenser and evaporator have been shown for increasing compressor frequency (ω) and different pre-heater temperatures (T_{heater}). However, in this case the heat flux input at the bottom of the evaporator (q_{in}) is kept constant by providing constant electrical power to the heater. All the heat flux q_{in} applied at the bottom of the evaporator is not transferred to the refrigerant as some amount of heat is lost. Wall heat flux, which is transferred to the refrigerant is q'', where $q'' < q_{in}$.

Wall heat flux (q'') depends on both compressor frequency and pre-heater temperature. The compressor used in the experiment is a variable speed compressor. The speed is varied by varying compressor frequency using a variable frequency drive. By changing compressor speed, mass flow rate is changed. For this reason, wall heat flux is changed. Higher frequency results higher refrigerant flow rate for which heat transfer rate increases. Hence, most of the heat flux applied at the bottom of the evaporator (q_{in}) is transferred to the refrigerant, which results increment of the wall heat flux q''.

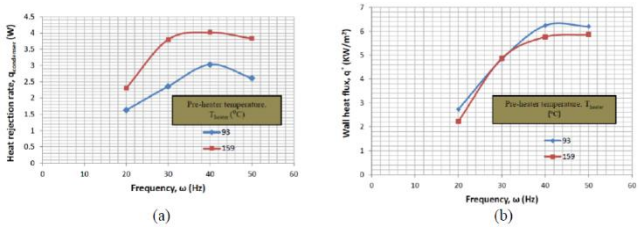


Fig 13: (a) Condenser heat rejection rate vs. frequency curve (b) Effective heat flux vs. frequency curve at different pre-heater temperatures (Constant heater power, q_{in} = 3.3 W)

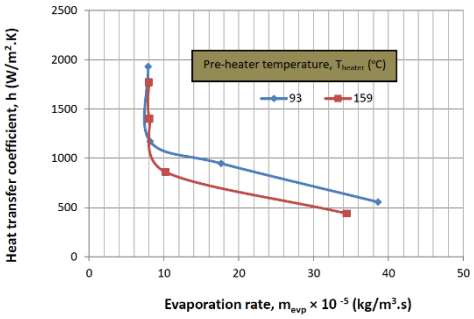


Fig.14: Evaporation rate vs. convective heat transfer coefficient at different pre-heater temperatures (Constant heater power, q_{in} = 3.3 W)

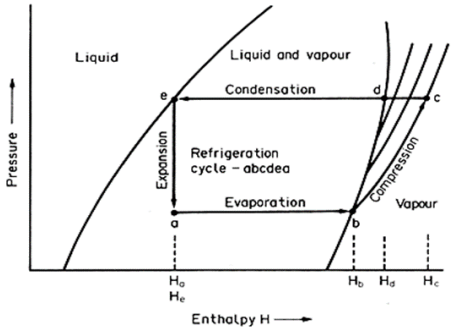


Fig.15: pressure-enthalpy diagram of the heat pump

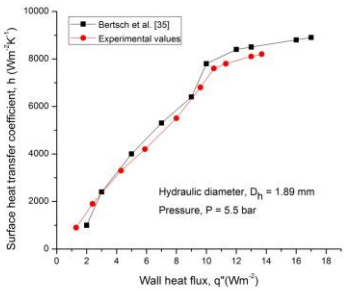


Fig. 16: Heat transfer coefficient vs. wall heat flux at 5.5 bar saturation pressure and 40 Hz compressor frequency

For pre-heater temperature of 159°C, frequency increment from 20Hz to 30 Hz results 118.2% increment in evaporator wall heat flux (q'') and 65.2% in heat rejection rate in the condenser ($q_{condenser}$). However, heat transfer rate declines after surpassing 30 Hz compressor frequency. At lower frequency and pumping power, evaporation rate (m_{evp}) is high, which declines with increasing voltage-to-frequency ratio (v/ω). As vapor possesses low heat transfer coefficient, convective heat transfer coefficient (h) is low at higher rate of evaporation, which is shown in Fig.14. It results low wall heat flux at lower operating frequencies. m_{evp} drops-off with increasing voltage-frequency ratio, which in turn augments

heat transfer rate. Again, augmenting pre-heater temperature from 93°C to 159°C, gives rise to heat rejection rate at the condenser while wall heat flux at the evaporator slightly decreases. It can be explained from conventional pressure-enthalpy diagram of vapor compression cycle (Fig. 15). It is elucidated from the diagram that for increasing refrigerant enthalpy in the condenser, vapor quality at the evaporator inlet increases. As heat transfer coefficient of vapor is low, wall heat flux declines for higher amount of vapor in the mixture.

In Fig. 16, surface heat transfer coefficient for different wall heat fluxes have been compared with Bertsch et al. [35]. It is observed that for same channel hydraulic diameter and saturation pressure (D_h = 1.89 mm, P_{sat} = 5.5 bar), experimental results matches well with Bertsch et al. [35].

7.2.4 Coefficient of Performance

In Fig.17, coefficient of performance (COP) is plotted against compressor frequency for different pre-heater temperatures. COP increases for increasing frequency from 20 Hz to 30 Hz and decreases for further frequency increment. At higher frequencies, compressor power consumption is high as the inverter maintains a constant voltage-frequency ratio to regulate the compressor with same torque. However, from Fig.13(b), it is comprehended that increment rate of wall heat flux declines after surpassing 30 Hz frequency. Decreasing trend of heat transfer rate at the evaporator with escalating power consumption is the reason of COP drop. Again, as discussed earlier, wall heat flux is lower for higher pre-heater temperature, apprehended in Fig.13(b). As a result, compared to 93°C pre-heater temperature, low COP was obtained for 159°C temperature.

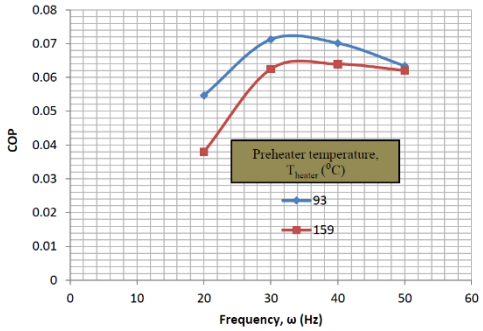


Fig.17: COP vs. frequency curve at different pre-heater temperatures

8. Conclusion

This study has been carried out to investigate flow boiling characteristics of R134a in a micro-finned micro-gap evaporator. Heat removal rates in micro-gap evaporator and condenser as well as coefficient of performance (COP) have been examined as a function of compressor frequency. At different frequencies, the compressor is operated with different powers to maintain a constant voltage-to-frequency ratio. The major findings are stated below:

1. Pseudo-turbulence in micro-gap is visualized in the numerical simulation. Turbulence intensity ratio improves greatly at the entrance and outlet of the evaporator due to fin induced pseudo-turbulence.

2. Quasi-periodic nature of dry out and surface rewetting explains the reason of temperature, flow rate and pressure fluctuations in transient state.

3. Heat transfer in evaporator and condenser are strongly influenced by compressor frequency. For pre-heater temperature of 159°C, wall heat flux escalates 118.2% for frequency increment from 20 Hz to 30 Hz. On the other hand, rate of heat loss in the condenser increases 65.2%. Coefficient of performance also augments.

4. It is observed that at higher operating frequencies, the increment of heat transfer rate is slow and COP even declines.

Acknowledgement

The support of International Islamic University Malaysia under the research grant RIGS17-033-0608 is gratefully acknowledged.

References

[1] Kakaç, S., Vasiliev, L. L., Bayazitoglu, Y., & Yener, Y. (Eds.). (2006). *Microscale Heat Transfer-Fundamentals and Applications: Proceedings of the NATO Advanced Study Institute on Microscale Heat Transfer-Fundamentals and Applications in Biological and Microelectromechanical Systems, Cesme-Izmir, Turkey, 18-30 July, 2004* (Vol. 193). Springer Science & Business Media.

[2] Bar-Cohen, A., Holloway, C., Kaffel, A., & Riaz, A. (2016). Waves and instabilities in high quality adiabatic flow in microgap channels. International Journal of Multiphase Flow, 83, 62-76.

[3] Tuckerman, B. & Pease, R.F.W, High-performance heat sinking for VLSI, *IEEE Electron. Dev. Lett. EDL-2*, (1981) pp.126 –129.

[4] Bertsch, S.S., Groll, E.A. & Garimella, S.V. (2009). Effects of heat flux, mass flux, vapor quality, and saturation temperature on flow boiling heat transfer in microchannels. *International Journal of Multiphase Flow*, 35(2), 142-154.

[5] Y. Wang, and K. Sefiane (2012). "Effects of heat flux, vapour quality, channel hydraulic diameter on flow boiling heat transfer in variable aspect ratio micro-channels using transparent heating," International Journal of Heat and Mass Transfer, vol. 55, no. 9, pp. 2235-2243, 2012.

[6] Yadigaroglu, G. (1978). Two-phase flow instabilities and propagation phenomena. *In Von Karman Inst. for Fluid Dyn. Two-Phase Flows in Nucl. Reactors, (SEE N79-28497 19-34) (Vol. 2)*, 71.

[7] Tadrist, L. (2007). Review on two-phase flow instabilities in narrow spaces. *International Journal of Heat and Fluid Flow*, *28(1)*, 54-62.

[8] Alam, T., Lee, P. S., Yap, C. R., & Jin, L., (2013). A comparative study of flow boiling heat transfer and pressure drop characteristics in microgap and microchannel heat sink and an evaluation of microgap heat sink for hotspot mitigation. *International Journal of Heat and Mass Transfer*, 58(1), 335-347.

[9] Kim, D. W., Rahim, E., Bar-Cohen, A., & Han, B. (2008, May). Thermofluid characteristics of two-phase flow in micro-gap channels. In *Thermal and Thermomechanical Phenomena in Electronic Systems, 2008. ITHERM 2008. 11th Intersociety Conference on* (pp. 979-992). IEEE.

[10] Bar-Cohen, A., & Rahim, E. (2007, January). Modeling and prediction of two-phase refrigerant flow regimes and heat transfer characteristics in microgap channels. In *ASME 2007 5th International Conference on Nanochannels, Microchannels, and Minichannels*, 1141-1160.

[11] Alam T., Lee P. S., Yap C. R., Jin L. W. & Balasubramanian K. (2012). Experimental investigation and flow visualization to determine the optimum dimension range of microgap heat sinks. *International Journal of Heat and Mass Transfer, 55(25)*, 7623-7634.

[12] Alam T., Lee P. S., Yap, C. R., & Jin, L. (2012). Experimental investigation of local flow boiling heat transfer and pressure drop characteristics in microgap channel. *International Journal of Multiphase Flow*, *42*, 164-174.

[13] Chang, W.R., Chen, C.A., Ke, J.H. & Lin, T.F. (2010). Subcooled flow boiling heat transfer and associated bubble characteristics of FC-72 on a heated micro-pin-finned silicon chip. *International Journal of Heat and Mass Transfer*, 53(23), 5605-5621.

[14] Yeom, T., Simon, T., Zhang, T., Zhang, M., North, M. & Cui, T. (2016). Enhanced heat transfer of heat sink channels with micro pin fin roughened walls. *International Journal of Heat and Mass Transfer*, 92, 617-627.

[15] Stehlík, P., Jegla, Z. & Kilkovský, B. (2014). Possibilities of intensifying heat transfer through finned surfaces in heat exchangers for high temperature applications. *Applied Thermal Engineering*, 70(2), 1283-1287.

[16] Ahmed, S., Ismail, A. F., Sulaeman, E. & Hasan, M. H. (2016a). A critical assessment on evaporative cooling performance of micro

finned micro gap for high heat flux applications. ARPN Journal of Engineering and Applied Sciences, vol. 11, no. 1, pp. 331-336.
[17] Ahmed, S., Ismail, A. F., Sulaeman, E., & Hasan, M. H. (2016b). A Comparative Analysis of Flow Boiling in Micro-Gaps with Internal Micro-Fins of Rectangular and Triangular Profiles. *International Journal of Applied Engineering Research*, *11*(4), 2364-2372.
[18] Ahmed, S., Hasan, M. H., Ismail, A. F., & Sulaeman, E. (2016c). Effect of geometrical parameters on boiling heat transfer and pressure drop in micro finned micro gap. ARPN Journal of Engineering and Applied Sciences, vol. 11, no. 1, pp. 297-302.
[19] Ahmed, S., Ismail, A.F., Sulaeman, E. & Hasan, M.H. (2016). Study on turbulent characteristics of flow boiling in a micro gap under the influence of surface roughness and micro fins. ARPN Journal of Engineering and Applied Sciences, vol. 11, no. 1, pp. 410-414, 2016.
[20] Hirt C. W. & Nichols B. D. (1981). Volume of fluid (VOF) method for the dynamics of free boundaries. *Journal of Computational Physics*. *39(1)*, 201–225.
[21] Brackbill J.U., Kothe D.B., Zemach C. (1992), A continuum method for modeling surface tension, *Journal of Computational Physics*, 100, 335-354.
[22] Orszag S. A., Yakhot V., Flannery W. S., Boysan F., Choudhury D., Maruzewski J. & Patel B. (1993). Renormalization Group Modeling and Turbulence Simulations. *International Conference on Near-Wall Turbulent Flows, Tempe, Arizona. 1031-1046.*
[23] Schrage, R. W. (1953). *A theoretical study of interphase mass transfer*. Columbia University Press.
[24] Lee, W. H. (1979), A Pressure Iteration Scheme for Two-Phase Modeling.*Technical Report LA-UR. Los Alamos Scientific Laboratory, Los Alamos, New Mexico*, 79 -975.
[25] Wu, H. L., Peng, X. F., Ye, P., and Gong, Y. E. (2007). Simulation of refrigerant flow boiling in serpentine tubes. *International Journal of Heat and Mass Transfer, 50(5)*, 1186–1195.
[26] De Schepper, S. C., Heynderickx, G. J. & Marin, G. B. (2009). Modeling the Evaporation of a Hydrocarbon Feedstock in the Convection Section of a Steam Cracker, *Computers & Chemical Engineering, 33(1)*, 122–132.
[27] Alizadehdakhel, A., Rahimi, M. and Alsairafi, A. A. (2010). CFD Modeling of Flow and Heat Transfer in a Thermosyphon. *International Communications in Heat and Mass Transfer, 37(3)*, 312–318.
[28] Patankar, S. V. & Spalding, D. B. (1972). A calculation procedure for heat, mass and momentum transfer in three-dimensional parabolic flows. *International Journal of Heat and Mass Transfer, 15(10)*, 1787-1806.
[29] Holman, J. P. (2001). Heat transfer, Eighth SI Metric Edition.
[30] Vlahostergios, Z., Missirlis, D., Flouros, M., Albanakis, C., & Yakinthos, K. (2015). Effect of turbulence intensity on the pressure drop and heat transfer in a staggered tube bundle heat exchanger. *Experimental Thermal and Fluid Science*, *60*, 75-82.
[31] Wang, G., Cheng, P., & Bergles, A. E. (2008). Effects of inlet/outlet configurations on flow boiling instability in parallel microchannels. *International Journal of Heat and Mass Transfer, 51(9)*, 2267-2281.
[32] Wu, H. Y., & Cheng, P. (2003). Visualization and measurements of periodic boiling in silicon microchannels. *International Journal of Heat and Mass Transfer, 46(14)*, 2603-2614.
[33] Hetsroni, G., Mosyak, A., Segal, Z., & Ziskind, G. (2002). A uniform temperature heat sink for cooling of electronic devices. *International Journal of Heat and Mass Transfer, 45(16)*, 3275-3286.
[34] Yin, L., Jia, L., & Guan, P. (2016b). Bubble confinement and deformation during flow boiling in microchannel. *International Communications in Heat and Mass Transfer, 70*, 47-52.
[35] Bertsch, S. S., Groll, E. A., & Garimella, S. V. (2008). Refrigerant flow boiling heat transfer in parallel microchannels as a function of local vapor quality. *International Journal of Heat and Mass Transfer, 51*(19-20), 4775-4787.